INTERNATIONAL JOURNAL OF HYDROGEN ENERGY 45 (2020) 34227–34240

Available online at www.sciencedirect.com

ScienceDirect

journal homepage: www.elsevier.com/locate/he

Effect of hydrogen on fracture locus of Fe–16Mn–0.6C–2.15Al TWIP steel

Burak Bal [a,*], *Barış Çetin* [b,c], *Ferdi Caner Bayram* [a], *Eren Billur* [d]

[a] *Department of Mechanical Engineering, Abdullah Gül University, 38080, Kayseri, Turkey*
[b] *FNSS Defense Systems Co. Inc., R&D Center, 06830, Ankara, Turkey*
[c] *Atılım University, Computational Science and Engineering Laboratory (CSE-Lab), 06830, Ankara, Turkey*
[d] *Atılım University, Department of Automotive Engineering, 06830, Ankara, Turkey*

HIGHLIGHTS

- Hydrogen degraded the mechanical properties regardless of the sample geometry.
- Hydrogen enhances the microstructural activities.
- Hydrogen affects fracture locus of TWIP steel significantly.
- Hydrogen reduces equivalent fracture strains at given stress triaxiality levels.

ARTICLE INFO

Article history:
Received 18 May 2020
Received in revised form
2 September 2020
Accepted 10 September 2020
Available online 29 September 2020

Keywords:
Hydrogen embrittlement
Tensile test
Fracture locus
TWIP steel
Johnson-cook failure model

ABSTRACT

Effect of hydrogen on the mechanical response and fracture locus of commercial TWIP steel was investigated comprehensively by tensile testing TWIP steel samples at room temperature and quasi-static regime. 5 different sample geometries were utilized to ensure different specific stress states and a digital image correlation (DIC) system was used during tensile tests. Electrochemical charging method was utilized for hydrogen charging and microstructural characterizations were carried out by scanning electron microscope. Stress triaxiality factors were calculated throughout the plastic deformation via finite element analysis (FEA) based simulations and average values were calculated at the most critical node. A specific Python script was developed to determine the equivalent fracture strain. Based on the experimental and numerical results, the relation between the equivalent fracture strain and stress triaxiality was determined and the effect of hydrogen on the corresponding fracture locus was quantified. The deterioration in the mechanical response due to hydrogen was observed regardless of the sample geometry and hydrogen changed the fracture mode from ductile to brittle. Moreover, hydrogen affected the fracture locus of TWIP steel by lowering the equivalent failure strains at given stress triaxiality levels. In this study, a modified Johnson-Cook failure mode was proposed and effect of hydrogen on damage constants were quantified.

---

* *Corresponding author.*
E-mail address: burak.bal@agu.edu.tr (B. Bal).

https://doi.org/10.1016/j.ijhydene.2020.09.083

Introduction

Development of materials having a superior combination of specific strength, ductility and toughness is the current trend in materials science. The advanced high strength steels (AHSSs) provide significantly improved strength and ductility over their conventional low strength counterparts [1–3]. The 1st generation AHSSs, e.g. dual phase, transformation-induced plasticity steels, show ultimate tensile strength (UTS) up to 1200 MPa with 25% total elongation, owing to the balance of soft ferrite, hard martensite, and metastable austenite. The 2nd generation AHSSs, high manganese steels, possess a superior combination of mechanical properties. For instance, high-Mn twinning-induced plasticity (TWIP) steel shows UTS of 1 GPa and ductility up to 80%. Lastly, the mechanical properties of recently developed 3rd generation AHSSs, Quenched and Partitioned (Q&P) steels and TRIP-aided Bainitic Ferrite steels, fall between the first and second generation AHSSs [4–6].

A key factor triggering the superior mechanical properties of TWIP steels is the low stacking fault energy (SFE). The low SFE assists dislocation separation, which enables occurrence of deformation twinning [7,8], dynamic strain aging (DSA) [9,10], and different microstructural interactions [11–13]. The tensile response of TWIP steel also exhibits jerky flow due to the DSA and Portevin-Le Chatelier (PLC) effects [14–16]. Relatively low stacking fault energy (SFE) triggers the simultaneous occurrence of different deformation mechanisms. In particular, enhanced partial dislocation separation in low SFE TWIP steel results in the ease of twin formation, which is an effective barrier to dislocation glide [17–19]. In addition, the effects of intercritical annealing temperature and alloying elements of the SFE, the key factor for controlling the TWIP and TRIP effects (austenite to hexagonal ε-martensite), have been well-documented [5,20,21]. Thereby, arranging the chemical composition and corresponding SFE accordingly, the dominancy of mechanical twinning, slip, stacking faults or phase transformation on the mechanical response can be arranged. Even though the primary deformation mechanism in austenite is dislocation glide, SFE values of TWIP steel are generally in between 12 and 40 mJ/m^2 so twin nucleation starts at the early stages of plastic deformation and they interact with other deformation mechanisms [8,22,23]. In addition, nano twin formation, secondary twin nucleation inside primary twins and corresponding Σ3 twin boundaries reduce the mean free path of dislocations and act as obstacles to dislocation motion [24,25]. With further contributions of DSA and PLC, TWIP steel achieves high strength and elongation values. However, TWIP steel has its own drawbacks such as, low yield strength, hydrogen embrittlement (HE) and delayed fracture [26–29]. In particular, they are not cost-effective for different applications due to their processing conditions, which triggers delayed fracture in TWIP steels. At first glance, TWIP steels look attractive material for hydrogen-related infrastructures due to their stable face centered cubic (FCC) structure, which provides low hydrogen diffusivity in the lattice compared to body centered cubic (BCC) structure, and their outstanding mechanical properties. On the contrary, it has been studied that ternary Fe–Mn–C TWIP steels are also vulnerable to HE, which is a severe environmental type of catastrophic failure and as the strength of a material increases, their susceptibility to HE also increases [30–33].

These shortcomings of TWIP steel have been studied widely in the literature. In particular, the effects of different alloying elements on mechanical response, austenite stability, delayed fracture and HE have been investigated comprehensively [21,34–36]. The main HE mechanisms of TWIP steel, including hydrogen enhanced localized plasticity (HELP), hydrogen enhanced decohesion (HEDE), adsorption induced dislocation emission (AIDE), and the effects of several factors, which are strain rate, twin density, martensitic transformability, hydrogen content, grain & twin boundaries characters, strain aging hardenability, load and stress states, on the HE susceptibility of TWIP steels have also been well-documented [37–40]. Another important problem, which limits TWIP steels' usage in different applications and very important for delayed fracture, is understanding and modelling damage evolution and ductile fracture of TWIP steels, both smooth and especially complex geometries, under different regimes. In terms of stress state, understanding plasticity-driven damage evolution and fracture of structural components with both smooth and especially complex geometries is practically important. Specifically, a strong plastic anisotropy, that occurs even without significant texture [41], increases the importance of the stress state effect. The applicable material and damage models for TWIP steels are Hill's anisotropic criterion [42], Johnson-Cook (JC) model [43] and criteria developed by Barlat et al. [44] and invariants of stress tensors are derived using a von Mises-based formalism [45]. However, to the best of authors' knowledge, there is no single study that sheds light onto both the hydrogen effect on fracture locus and the effect of geometrical constraints on HE susceptibility of TWIP steel at continuum level considering the microstructure evolution. The studies are generally focused on either the effect of stress state by performing notched tensile tests to hydrogen-charged samples together with other factors (strain rate, hydrogen source, etc.) or material and damage modelling of hydrogen free TWIP steels [45–48]. There are only a limited number of studies that combine these two important phenomena in different materials. For instance, a critical-strain criterion for HE of cold-drawn ultrafine pearlitic steel was proposed [49], fracture criterion for HE of boron bearing low alloy steel was proposed [50], stress based failure criterion law including the hydrogen degradation law on critical stress was studied for AISI 4135 high strength steel [51,52]. Lastly, there are several studies that incorporate the effect of HE by utilizing cohesive zone modelling (CZM) technique and modified traction separation law [53,54]. In these studies, HELP and HEDE concepts were implemented by lowering the cohesive strength and the separation energy due to atomic hydrogen.

In the present work, the effect of hydrogen on the fracture locus of TWIP steel was investigated comprehensively by tensile testing TWIP steel samples, having specific stress states, at ambient temperature. During tensile tests, a digital image correlation (DIC) system was used to analyze the localized deformation and calculate the equivalent fracture strain. By means of these valuable experimental data, the JC failure model parameters (D1, D2 and D3) were also extracted for the hydrogen-uncharged and hydrogen-charged TWIP steels. In addition, to elucidate the effects of stress state on HE susceptibility of TWIP steel, the microstructural investigations were carried out via scanning electron microscopy (SEM), energy dispersive x-ray spectroscopy (EDX) and X-ray diffraction (XRD).

Material and method

As received material

In the present study, a polycrystalline TWIP steel, prepared by vacuum induction melting, was investigated and its chemical composition is given in Table 1. The material was solution heat treated at in an electric furnace to obtain a fully recrystallized microstructure and water quenched. The initial microstructure was austenite and the grains were randomly oriented. The texture measurements were carried out with a Bruker D8Discover X-ray diffractometer using copper anode, Cu Kα, radiation (wavelength = 1.5406 Å). Fig. 1 shows the XRD data of the tested materials. Only austenite peaks were found in the tensile tests' specimens and no martensite peaks were observed. The data were collected over a range of 20°–100° in 2θ and the XRD was operated at 40 kV accelerating voltage and a scanning speed of 2° min^{-1}. The initial microstructure was also observed using scanning electron microscope (SEM, Zeiss Gemini 300).

Hydrogen charging, tensile tests and microstructural characterization

All test specimens were mechanically grinded and chemically polished by standard grinding and polishing metallographic equipment to remove all surface defects and residual stresses, and then etched with 8% Nital solution. The grain sizes of the specimens were measured by the linear intercept method using optical micrographs and the specimens had an initial linear intercept grain size of 10.50 μm. Hydrogen was introduced into the specimens by electrochemical charging before tensile tests at 353 K in a 3% NaCl aqueous solution containing 3 g/L NH_4SCN at the current density of 100 A/m^2 for 72 h. A platinum (Pt) wire having nearly 3 mm^2 surface area was used as the auxiliary (counter) electrode. The schematic representation of our hydrogen-charging setup is given in the supplementary files of our previous study [55]. The solution was changed every 12 h and the specimen surfaces were mechanically polished to remove contamination layer due to hydrogen charging. For these conditions, it was observed that hydrogen diffused up to 200 μm via hydrogen diffusion modelling, where hydrogen diffusion coefficient was taken as 1.02*10^{-8} [56], and no surface damage was observed after hydrogen charging. The details of hydrogen diffusion modelling were explained in our previous study [55] and the hydrogen-affected depth correspond well with experimental results published in the literature [38].

Table 1 – Chemical composition of the material studied (in wt.-%).

Mn	Al	C	Si	P	S	Fe
16.1	2.15	0.6	0.64	<0.001	<0.01	Balance

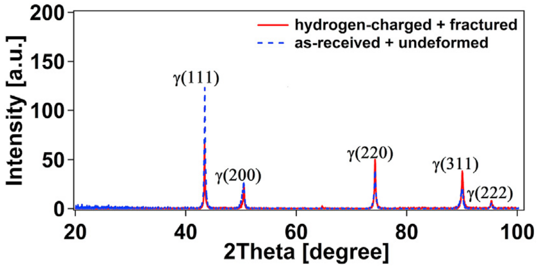

Fig. 1 – The XRD patterns of as-received and hydrogen charged + fractured TWIP steel samples.

Tensile specimens were extracted from the bar by electric discharge machining (EDM). 5 different sample geometries (Fig. 2) were selected to ensure different stress triaxialities and predict the effect of hydrogen on corresponding fracture locus and the notches were also introduced using EDM technique. Tensile tests were conducted on an Instron 8801 tensile testing machine with a constant crosshead speed of 0.009 mm/s at room temperature with and without hydrogen charging. This crosshead speed was slow enough to promote HE by giving enough time for atomic hydrogen to interact with dislocations. For hydrogen-charged specimens, tensile tests were conducted right after hydrogen charging to prevent any possible hydrogen back diffusion. During all tensile tests, the DIC system was utilized to analyze the localized deformation occurring within the gauge of the specimens and to determine the equivalent fracture strain. The surface of the deformed and fractured specimens was examined by scanning electron microscope (SEM) and EDX and corresponding microstructure and the effect of hydrogen on the fracture surface has been revealed.

Development of the JC based damage model

Regarding the ductile fracture of metals, the fracture strain is dependent on the hydrostatic stress, which means that it changes with respect to the stress state. This fact is theoretically proven and experimentally demonstrated previously by many researchers [57–60]. The JC damage model which is embedded to most of the non-linear FEA commercial software also proposes an exponentially decaying function between the stress triaxiality factor (STF) and the equivalent fracture strain, at the reference strain rate and temperature condition as explicitly expressed in Eq. (1), where ε_f is the equivalent fracture strain, η is the STF and D_1, D_2, D_3 are the material parameters [61].

$$\varepsilon_f|_{\dot{\varepsilon},T} = D_1 + D_2 * e^{D_3 * \eta} \tag{1}$$

In this contribution, aiming to determine the fracture locus (STF versus eq. fracture strain plot) of the studied TWIP steel, tensile specimens having specific notch dimensions were used. Thus, multi-axial stress states were obtained in the tensile testing, each representing a specific STF, which is explicitly expressed in Eq. (2), where $\sigma_{eq}, \sigma_{mean}$, σ_{11}, σ_{22} and σ_{33}

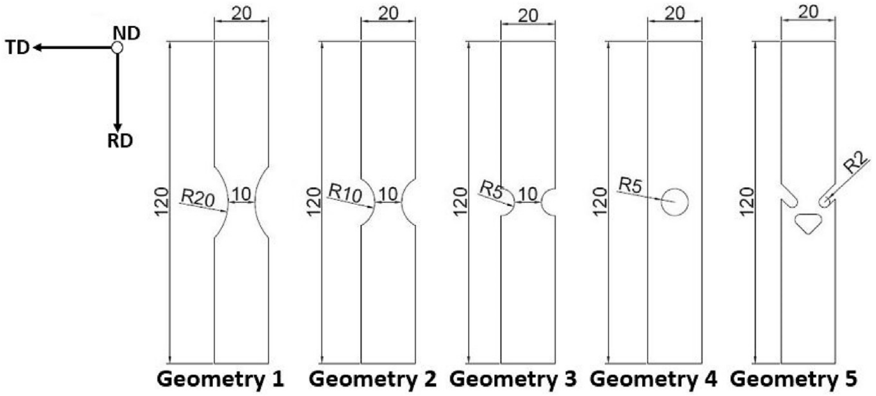

Fig. 2 – Specimen dimensions for tensile testing (unit: mm).

represents the equivalent stress, mean stress (hydrostatic stress) and diagonal components of the Cauchy stress tensor, respectively.

$$\mathrm{STF} = \frac{\sigma_{mean}}{\sigma_{eq}} = \frac{(\sigma_{11} + \sigma_{22} + \sigma_{33})/3}{\sigma_{eq}} \tag{2}$$

As in the pioneering study of Bridgeman, it is possible to create analytical expressions of STF depending on the specimen geometry, however, these approaches generally use highly questionable assumptions such as perfect plastic material behavior [62]. Moreover, it is also shown that STF is not constant throughout the plastic deformation process and it has also a spatial distribution [59,63]. To overcome this fact, it is necessary to conduct finite element analysis (FEA) based simulations and perform an averaging process for the most critical node (the central node of the notched cross-section) to determine the nominal STF in a more scientifically meaningful manner. For that purpose, five FEA models were constructed in MSC Marc software. The models totally represent the tensile tests and the components of Cauchy stress tensor and equivalent plastic strain values were extracted from the post-processor to define the evolution of STF (Fig. 5). A sample of the meshing structure of the specimen having a 10 mm notch radius is illustrated in Fig. 3. Since the tensile specimens have a thickness of 1.0 mm, 4-node quadrilateral linear and full integration plane stress elements (element type-3 in MSC Marc)

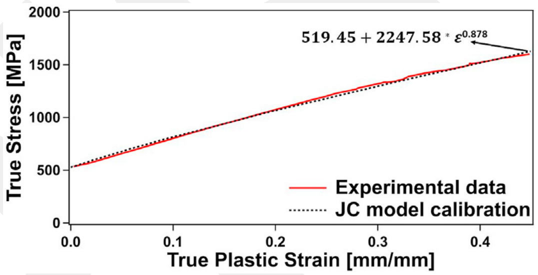

Fig. 4 – True stress – true plastic strain of the studied TWIP steel.

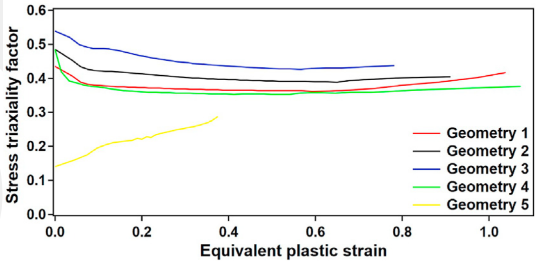

Fig. 5 – Evolution of the STF with respect to equivalent plastic strain.

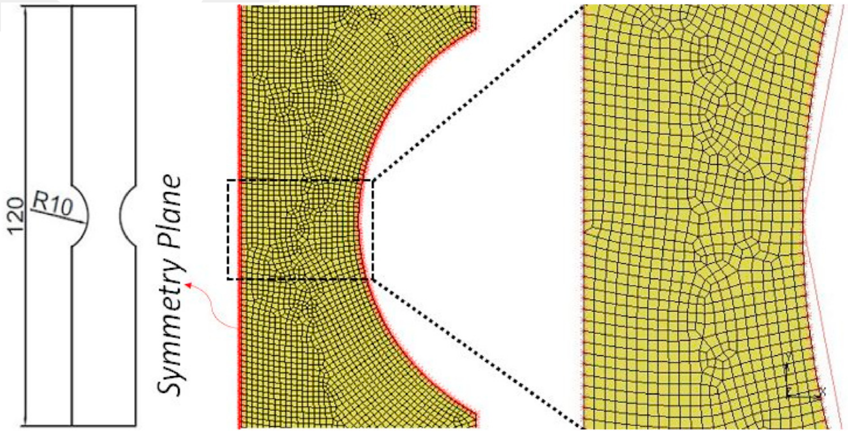

Fig. 3 – Meshing structure of the specimen having a 10 mm notch radius.

were used in the FEA models with an average element size of 0.50*0.50 mm. Due to the nature of the tensile test, ½ symmetricity approach was used in the simulations, as can be seen in Fig. 3. All the simulations were run regarding the J2-plasticity theory (Von Mises's yield criteria) and isotropic hardening assumption with finite strain theory. The flow curve data of the studied steel is given in Fig. 4. This data is obtained from a conventional tensile test with an initial gauge length of 80 mm and gauge width of 20 mm in rolling direction.

In Fig. 5, the evolution of the STF values was depicted for each geometry to the limit of the maximum equivalent plastic strain obtained in the tensile tests. Then, with respect to Eq. (3) the nominal (average) STF values for each tensile specimen were determined and listed in Table 2. In Eq. (3), η and $\overline{\varepsilon}_p$ are representing the STF and equivalent plastic strain respectively and this integral was calculated up to the equivalent failure strain of each tensile test, as previously explained.

$$\eta = \left(\frac{1}{\overline{\varepsilon}_p}\right) * \int_0^{\overline{\varepsilon}} \eta(\overline{\varepsilon}_p) * d\overline{\varepsilon}_p \tag{3}$$

As shown in Fig. 5, apart from the sample with Geometry-5, STF slightly drops at the beginning of the plastic deformation and then reaches nearly the steady state. As the Geometry-5 is a tensile-shear specimen, its STF values should be the lowest one which corresponds well with the FEA results. Furthermore, Geometry-4 represents a standard tensile specimen, whereas for the rest of the specimens, tension-compression stress state is valid. Enlarging the notch radius gradually increases the hydrostatic stress at the notched region which leads to higher STF values by causing high stress localization and local strain hardening tendency [64,65]. Therefore, due to the nature of the geometries, STF of the Geometry-4 should be near to 1/3 and it should increase through Geometry-1 to Geometry-3. Under these circumstances, it is concluded that the STF values obtained from FEA based simulations nicely agree well with the theoretical expressions and the previous studies [59,62]. It is also worth here to remark that the existing geometries provided the experimental data in the medium STF range.

Digital image correlation (DIC) setup

Ncorr [66], which is a powerful and open source MATLAB-based program, was utilized in order to perform the DIC analysis for calculating the equivalent fracture strain of each geometry. To do this, firstly random speckle patterns were established by spraying black paint solution on specimen surface. Before creating black speckle pattern on specimen surface, white paint solution was used to color background of each geometry to obtain a smooth surface. Creating a random speckle pattern is vital for correlation analysis due to proper image tracing during Ncorr analysis. All the tensile tests were recorded with 4 K resolution until failure and 120 images were extracted from each video by using DVDVideoSoft Free Studio software. Then, these images were sent to Ncorr and processed with the proper subset and reference of interest (ROI) dimensions. By the end of the DIC analysis, Ncorr output the in-plane Green-Lagrangian strains as $\varepsilon_{xx}, \varepsilon_{yy}$ and ε_{yx}. The obtained Green-Lagrangian strain values were used to define principal strains $\varepsilon_{11}, \varepsilon_{22}$ through Eq. (4.1). Then, the obtained principal strains were converted to true (Hencky) strains through Eq. (4.2). (For the details of Eq. (4.2), please refer to appendix). The third component of the true principal strain (ε_{33}) was computed with the volume consistency assumption of J2-plasticity theory.

Table 2 – Nominal STF and equivalent fracture strain values of each h-uncharged and h-charged tensile specimen.

	STF	Equivalent Fracture Strain	
		Hydrogen-uncharged	Hydrogen-charged
Geometry 1	0.3740	0.5496	0.3838
Geometry 2	0.4063	0.5109	0.3193
Geometry 3	0.4552	0.4742	0.2536
Geometry 4	0.3662	0.5699	0.4058
Geometry 5	0.2390	0.2796	0.1561

$$\varepsilon_{11,22} = \frac{\varepsilon_{xx} + \varepsilon_{yy}}{2} \pm \sqrt{\left(\frac{\varepsilon_{xx} - \varepsilon_{yy}}{2}\right)^2 + \left(\varepsilon_{xy}\right)^2} \tag{4.1}$$

$$\varepsilon_{true} = \ln\left(\sqrt{2 * \varepsilon_{lang} + 1}\right) \tag{4.2}$$

Finally, the Von Mises equivalent strain equation, explicitly given in Eq. (5), was used to determine equivalent fracture strains, ε_f.

$$\varepsilon_f = \sqrt{\left({}^{2}\!/\!{}_{3}\right) * \left(\varepsilon_{11}^2 + \varepsilon_{22}^2 + \varepsilon_{33}^2\right)} \tag{5}$$

Through DIC analysis, there is also an important challenge to be surmounted that Ncorr generally yields the strain field data and specifically the mean strain which is the overall average of the ROI. From this perspective, the mean strain is particularly far away from the equivalent fracture strain intended to be computed. Seymen et al. has previously used the mean strain values in determining the fracture strains by means of special set-up which focuses on a very small spot area with the help of the 20× objective lenses [67]. However, the ROI in the current study is larger. Therefore, a specific Python script was developed in the present study which inputs the strain field and the color bar by using rgb decomposition individually. The script then performs a computation for the highest strained section (HSS) which is an input from the user. In particular, the script computes the strain values of each pixel which is located on HSS and determines the mean strain. In Fig. 6, the reference image and results data of the Python scripts for the hydrogen-uncharged Geometry-1 sample are displayed.

Results and discussion

Effect of hydrogen on the mechanical response

Fig. 7 shows the engineering stress vs displacement curves of the TWIP steels with different sample geometries and with and without hydrogen charging at room temperature. The mechanical responses of TWIP steel at cross head

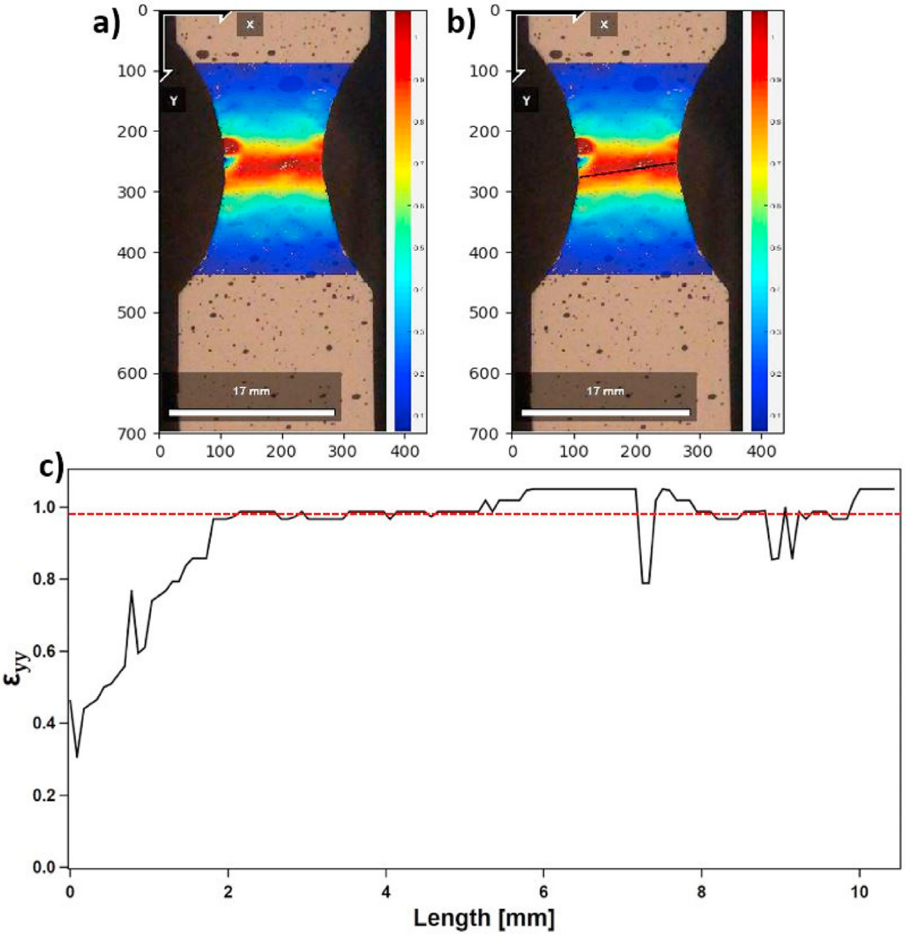

Fig. 6 — a) Reference image taken from Ncorr for ε_{yy} b) the reference image in Python script with HSS (black line), c) ε_{yy} of each pixel on HSS vs length graph (mean strain: 0.980).

displacement speeds of 2.5 mm/s and 9×10^{-3} mm/s are given in Fig. 7a and b, respectively. It can be clearly seen that HE is pronounced at low cross head displacement speed. Therefore, the rest of the experiments were conducted at low cross head displacement speed, 9×10^{-3} mm/s. The serrations, given as an inset of each figure, in the material response arise from DSA [41,68,69] and it was observed that atomic hydrogen suppressed the occurrence of DSA and this observation is in accordance with previous DSA observations in TWIP steels [32,37]. From geometry 1 to geometry 5, hydrogen charging deteriorated the elongation of TWIP steel by 32%, %27, 36%, 54% and 27%, respectively. Yield strength (YS) was calculated through 0.2% offset method (Proof stress). It was observed that, yield strengths of the specimens (each geometry) were not affected by hydrogen charging significantly even though it deteriorated the elongation at failure drastically. Similar observations in TWIP steel were also reported before [32,70]. Changing the sample geometry altered the mechanical response even without hydrogen charging. In particular, a slight decrease in elongation at failure was observed from geometry 1 to geometry 3 (Fig. 7b–d). This decrease can be attributed to the fact that sharper notch (Fig. 7d) results in greater stress concentration, which accelerates the crack growth compared to smoother notch (Fig. 7b and c) [71,72]. Introducing further discontinuities (Fig. 7e and f), resulting in more stress concentration, deteriorated both the elongation and strength values dramatically. Especially in geometry 5, plastic deformation was localized in two main regions, resulting in inhomogeneous plastic flow (Fig. 7f). Once, the stress concentration could not be accommodated plastically by one region tearing took place and abrupt decrease in flow stress was observed until the remaining region ruptured (Fig. 7f) [73]. In addition, hydrogen decreases the stress level of some specimens (Fig. 7c, e and f). Decrease in flow stress due to hydrogen was also observed previously in TWIP steels [37,74] whereas few studies state hydrogen enhanced flow stress in different materials including TWIP steels [41,75,76]. This controversy arises from whether hydrogen can pin the dislocations like carbon atom and be utilized for beneficial strengthening and toughening mechanism or it reduces the barriers against dislocation motion and enhances dislocation mobility (HELP mechanism) and it was concluded that proper hydrogen concentration might increase the strength of a material depending on the microstructure [76].

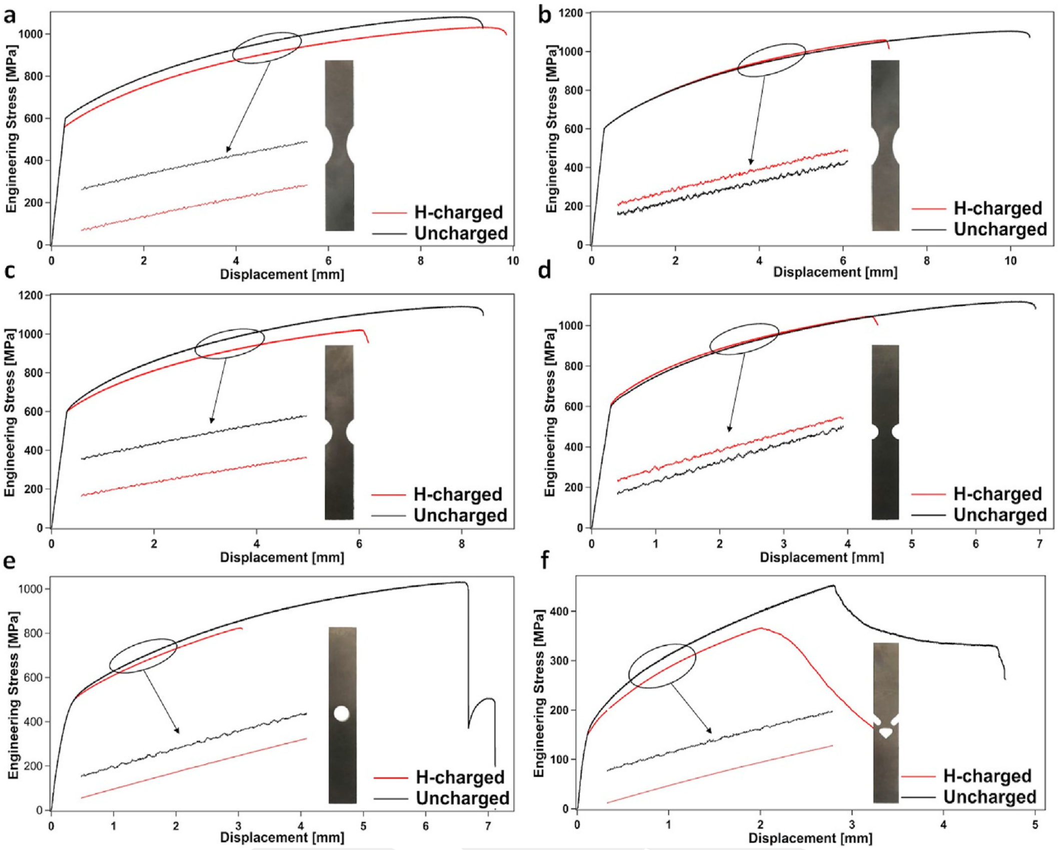

Fig. 7 – Engineering stress–displacement curves of hydrogen-charged and uncharged TWIP steels.

Effect of hydrogen on the fractographic features

Fig. 8 shows the in-situ SEM micrograph of hydrogen-uncharged TWIP steel (Geometry-1) after 6 mm deformation along the tensile direction at a deformation rate of 0.009 mm/s. Voids and elongated inclusions, which is a ductile fracture mechanism, can be clearly observed in Fig. 8a. Fig. 8a1 is the magnified micro image of the highlighted region in Fig. 8a. Slip traces and twins can be seen in Fig. 8a1 and a2. In particular, twinning occurs on different planes (Fig. 8a2). Previous studies

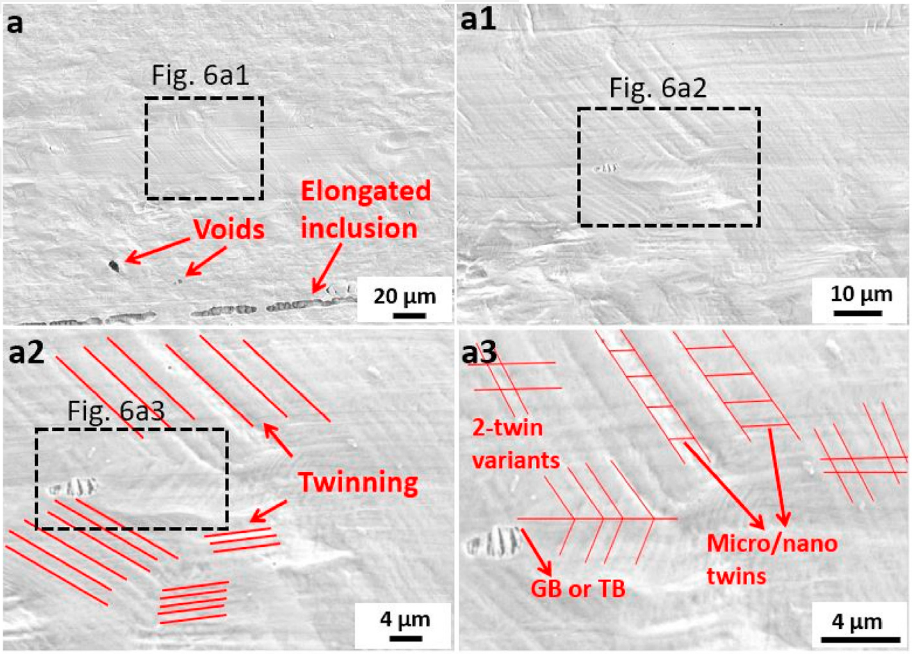

Fig. 8 – In-situ SEM micrograph of Geometry-1 without hydrogen charging after 6 mm deformation at 0.009 mm/s.

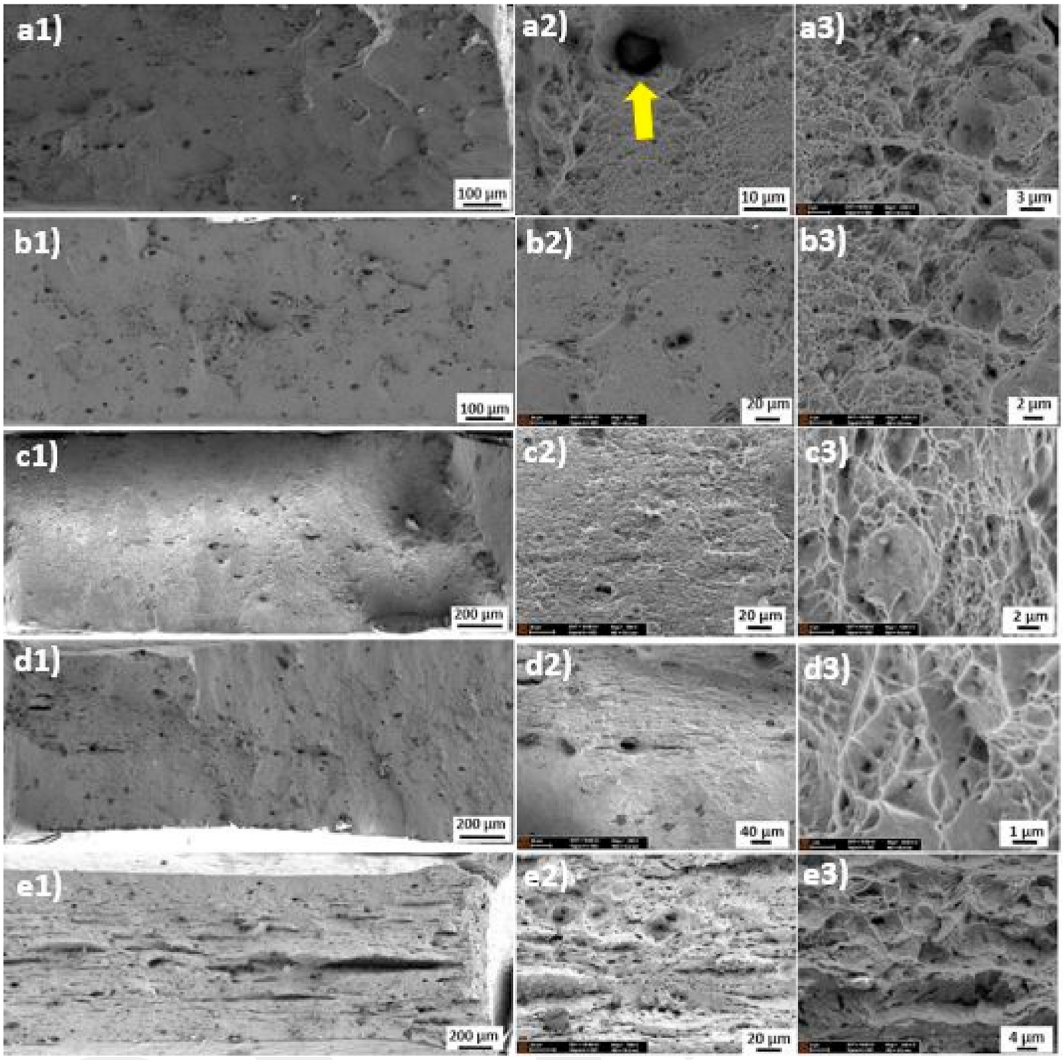

Fig. 9 – Fracture morphologies of five different hydrogen-uncharged tensile test specimens (refer to Fig. 2): (a1) Geometry 1, (a2) Geometry 2, (a3) Geometry 3, (a4) Geometry 4, (a5) Geometry 5. (a2) and (a3) are the magnified images of (a).

have demonstrated that even though {111} is the most favorable twin plane, other planes can be active during deformation in austenitic TWIP steels [77,78]. Moreover, two different twin variants and micro/nano twin formation within the previously formed twins were observed (Fig. 8a3). Also, slip bands and twins impinge at grain or twin boundaries, which creates additional stress or plastic strain concentration. Formation of different twin variants and micro/nano twins inside previously formed twins are common observation in TWIP steels and aforementioned microstructural events were well discussed in the literature and the current observations well with previous findings [12,13,19]. It was also shown previously that hydrogen enhances the microstructural activities in TWIP steels at all strain levels [41], thereby hydrogen-charged specimens should have more microstructural interactions, which contribute the HE mechanism by creating local stress concentrations and distorting the twin boundaries, than hydrogen-free specimens. In addition, neither γ (fcc) to ε (hcp) nor γ (fcc) to α' (bcc) phase transformation was observed in XRD results (Fig. 1), which might be attributed to stacking faults were superposed on every second closest paced $(111)_\gamma$ of the austenite structure [79–81]. Therefore, the main failure and/or HE mechanism in the current study is not related to phase transformation induced boundary cracking but related to enhanced microstructural activities and corresponding cracking.

Figs. 9 and 10 show the fracture surfaces of the hydrogen-uncharged and hydrogen-charged specimens, respectively. The fracture surfaces were observed by SEM after fracture and the corresponding images were taken from the fracture edge of notches and different magnifications are also included in Figs. 9a2 and a3 and 10a2 and a3 in order to illustrate the morphology characteristics upon closer inspection. It can be seen in Fig. 9 that the fracture surfaces of hydrogen-uncharged specimens (Geometry 1 to 4) were characterized by very fine dimples with a wide range of sizes resulting from the characteristics of ductile fracture which are the void nucleation, growth and coalescences of these micro-sized voids as plastic strain increases. Inclusions were found in some dimples, suggesting that inclusions (shown by yellow arrow) were the initiation sites for microvoid coalescence

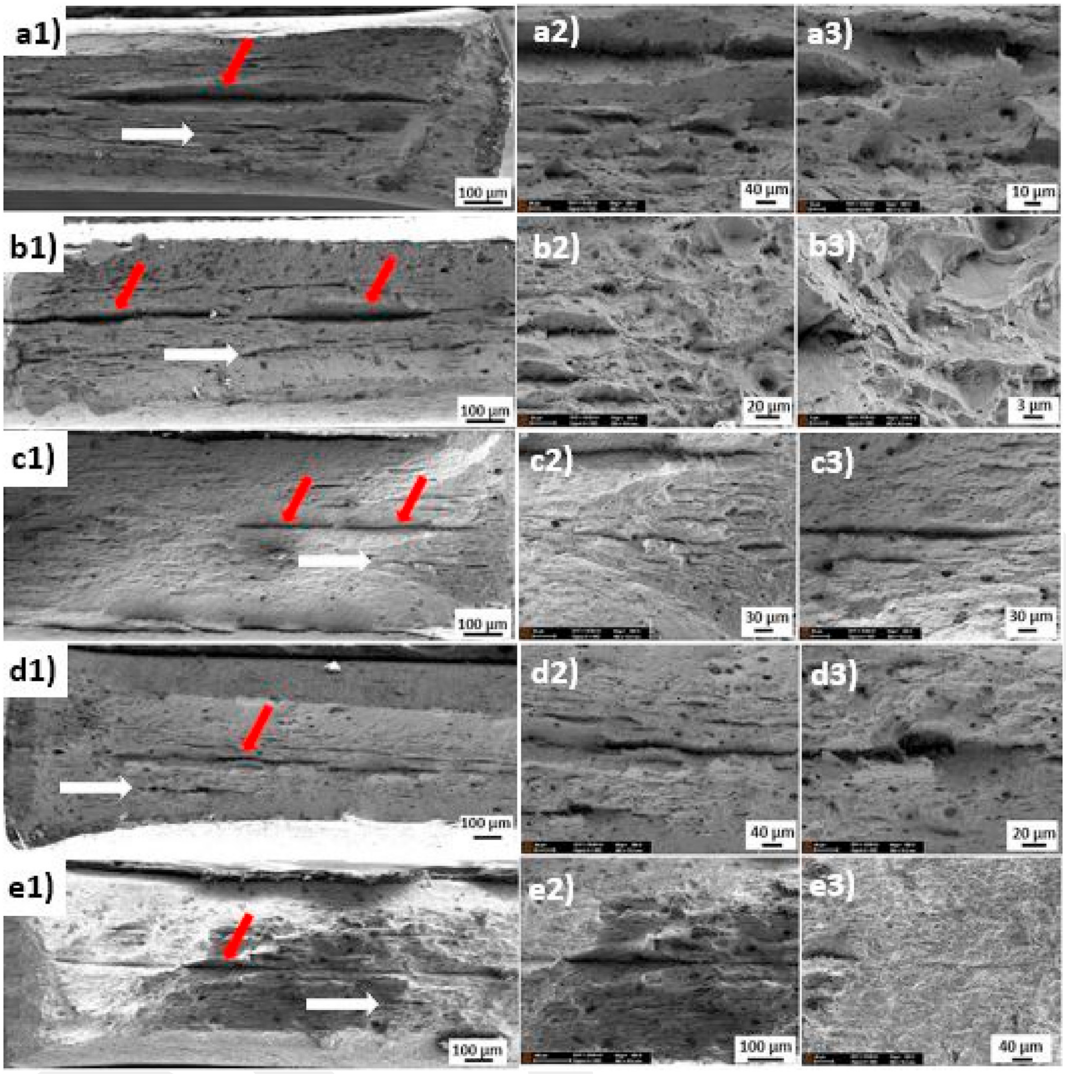

Fig. 10 – Fracture morphologies of hydrogen-charged tensile test specimens conducted at 0.009 mm/s and at five different geometries (refer to Fig. 2): (a1) Geometry 1, (a2) Geometry 2, (a3) Geometry 3, (a4) Geometry 4, (a5) Geometry 5. (a2) and (a3) are the magnified images of (a).

(MVC), which agrees well with the literature [82,83]. In contrast, hydrogen changed the fracture mode from a ductile, MVC failure to brittle transgranular fracture with clear deep cracks (shown by red arrow) with the crack size of more than 200 μm and secondary cracks (shown by white arrow) regardless of sample geometry (Fig. 10). This finding is consistent with the results obtained from previous studies on different materials and also TWIP steels [30,84]. The localization of transgranular fracture at the center of the surface confirmed that the hydrogen was able to diffuse up to the center of the tensile specimens. The hydrogen was most probably transport from the surface to the center via simple diffusion as well as dislocation motions. Hydrogen assisted cracking is very well discussed phenomenon in the literature and the current results are also strengthening this event [38]. The possible causes for transgranular fracture are hydrogen enhanced microstructural events (slip and deformation twinning as well as slip-twin interactions), the dislocation accumulation that forms cell walls and reduction in cohesive energy of grain boundaries due to hydrogen [33,38,74,85,86]. At higher magnifications (Fig. 10a3–10e3), the fracture surfaces presented dimple mixed with quasi-cleavage fractures, which can be explained by HELP and AIDE mechanisms [87–89]. In geometry 5, since there were two different fracture regions due to the anisotropy, the one fractured first was examined via SEM as that is a critical region and brittle fracture with primary and secondary cracks were observed even before hydrogen charging (Fig. 9e1).

Effect of hydrogen on the fracture locus

Even though the JC damage criterion foresees an exponential decaying function as previously mentioned, generally in the shear-dominant failure modes ($0 \le \eta \le 1/3$) the behavior of metals alters notably. This fact is also valid for the negative STF regimes i.e., compressive stress states. For instants, Bao and Wierbiczkzi has previously showed that in the case of Al 2024-T351 alloy, there is a highly different fracture behavior in

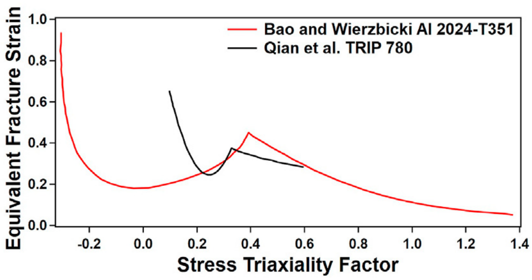

Fig. 11 – Fracture locus of Al 2024-T351 and TRIP-780 steel (data recompiled from Ref. [90,91]).

low and high STF ranges where the uniaxial tension stress state ($\eta = 1/3$) behaves like a critical point [90]. Similarly, Qian et al. obtained close experimental results as Bao and Wierbiczkzi for TRIP 780 steel [91]. The fracture loci obtained from those two studies is displayed in Fig. 11.

Fig. 12a shows the experimentally obtained fracture locus of the hydrogen-charged and hydrogen-uncharged Fe–16Mn–0.6C–2.15Al TWIP steels. There are three important findings that could be drawn: (i) the JC damage model prediction also suffers for the studied material. If one uses the whole data points, the curve fit performance (D1, D2 and D3 parameters) will be highly poor which means any FEA based predictions may include high margins of error. On the other hand, if the low STF regime is ignored, the experimental data fits perfectly ($R^2 \approx 0.99$) for the high STF regime however this JC damage parameter set definitely overshoots the fracture strain in low STF regime. This fact was schematically depicted in a detailed manner in Fig. 12b. (ii) Since the region under the fracture locus means rupture-free plastic deformation, hydrogen has a drastic effect on the formability of Fe–16Mn–0.6C–2.15Al TWIP steel by lowering the fracture locus approximately 37%. This finding also emphasizes the importance of mitigating of any possible HE risks is very valuable in assuring defect-free forming process of TWIP steel. (iii) Finally, it was also observed that the amount of the formability degradation in different stress states have a dispersion to some extent. However, in the high STF regime it is observed that higher STF values yield higher percentage reduction in eq. fracture strain. This finding could be explained as at high STF values (high hydrostatic stress) coexistence of different HE mechanisms can be observed. We intend to investigate this fact in a more detailed manner as a future work by deepening the subject with more advanced microstructural analysis. In Table 3, the percentage reduction in the equivalent fracture strain due to hydrogen with respect to STF is given.

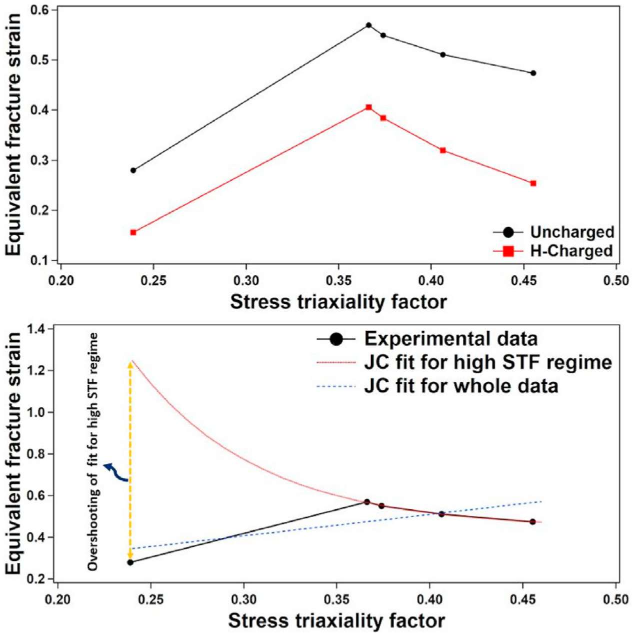

Fig. 12 – a) Fracture locus of the hydrogen-charged and uncharged Fe–16Mn–0.6C–2.15Al TWIP steels. b) Prediction performance of JC damage model curve fit with different alternative approaches for Fe–16Mn–0.6C–2.15Al TWIP steels.

Modified Johnson-Cook based fracture locus definition and final remarks

It was concluded from the experimental studies that the JC damage criterion (Eq. (1)) is lack of capturing the fracture locus of hydrogen-uncharged or hydrogen-charged Fe–16Mn–0.6C–2.15Al TWIP steels with high precision. For that reason, a modified fracture locus definition was proposed to provide a more realistic FEA simulation in Eq. (6). In that sense, low STF regime is assumed in a linear way and the high STF was modeled through the JC damage criterion. For instance, this approach yields to a fracture locus of the hydrogen-uncharged Fe–16Mn–0.6C–2.15Al TWIP steel which is defined in a step function manner as in Eq. (6).

$$\begin{aligned} \varepsilon_f &= D_1 + D_2 * \eta && \text{if } \eta < \eta_{crit} \\ \varepsilon_f &= D_3 + D_4 * e^{D_5 * \eta} && \text{if } \eta \geq \eta_{crit} \end{aligned} \tag{6}$$

In Eq. (6), η_{crit} is the critical STF, which represents the transition from low STF to high STF. Modified JC damage parameters for the hydrogen-uncharged and hydrogen-charged Fe–16Mn–0.6C–2.15Al TWIP steels is given in Table 4. Due to the fact that current study basically focuses on the effect of HE on the mechanical response and fracture locus of Fe–16Mn–0.6C–2.15Al TWIP steel, at this point it would be slightly out of scope to create a novel damage evolution rule. Here, the authors have just created a novel fracture locus definition as a step function and intend to determine a whole constitutive equation and a novel damage criterion and damage evolution rule of TWIP steels in hydrogen-uncharged and hydrogen-charged conditions as a future work. In that future study, we will also focus on low STF region specifically

Table 3 – Percentage decrease in the fracture strain originated by HE with respect to STF.

Sample Geometry	STF	Percentage Reduction (%)
Geometry-1	0.3740	30.16
Geometry-2	0.4063	37.50
Geometry-3	0.4552	46.52
Geometry-4	0.3662	28.79
Geometry-5	0.2390	44.18

Table 4 – Johnson-Cook damage model parameters of H-uncharged and H-charged Fe–16Mn–0.6 TWIP steels.

	D_1	D_2	D_3	D_4	D_5	η_{crit}
H-uncharged	−0.266	2.282	0.441	28.000	−14.780	0.374
H-charged	−0.3131	1.960	0.157	11.860	−10.560	0.374

by machining more specimens within the low STF region by the help of which constructing more complex, such as exponential decaying or high order polynomial based, analytical expression would be possible.

Conclusion

In this study, the effects of hydrogen on the mechanical response, and fracture locus of Fe–16Mn–0.6C–2.15Al TWIP steel were investigated at room temperature and quasi-static regime. Tensile tests were conducted to 5 different sample geometries, ensuring different specific stress states and STF, and a DIC system was used during tensile tests. Corresponding fractographic investigations were carried out via SEM. From the work presented herein the following conclusions can be drawn:

1) Hydrogen degrades the mechanical properties of Fe–16Mn–0.6C–2.15Al TWIP steel regardless of the sample geometry. In particular, the effect of hydrogen on the flow curve of each tensile specimen is not much dominant, however there is a dramatic decrease in the maximum percentage elongation values. This finding could be interpreted as hydrogen does not have a remarkable influence on the plastic behavior in given STF regime apart from the onset of the fracture and ultimate tensile strength.
2) Hydrogen enhanced the microstructural activities and changed the fracture mode from a ductile failure to brittle transgranular fracture with clear deep cracks which is in well agreement with the experimentally observed ductility loss.
3) Hydrogen affects fracture locus significantly. Specifically, it reduces equivalent fracture strains for all the given stress triaxiality levels. An average decrease in the equivalent failure strain is approximately 37% which corresponds to a drastic degradation in formability of the studied steel due to hydrogen embrittlement. Moreover, the percentage reduction in equivalent fracture strain increases concurrently with increasing STF in tension-compression stress states which is a significant observation and to be investigated deeply as a future work.
4) A modified JC based fracture loci were proposed and hydrogen effect on the corresponding damage constants was numerically given in Table 4. This data set may provide a crucial input in defining a user-defined damage model for H-uncharged and H-charged conditions of the studied steel.

Declaration of competing interest

The authors declare that they have no known competing financial interests or personal relationships that could have appeared to influence the work reported in this paper.

Acknowledgments

The authors would like to acknowledge Asst. Prof. Dr. Hüseyin Kurtuldu from Baskent University for taking part in the preparation of Python script. The grain size measurement was conducted by means of Automet software which was developed PSARON HTI company. The authors also thank to Psaron company for the use of their software facilities. The authors acknowledge the support by the Scientific and Technological Research Council of Turkey (TÜBİTAK, Project No: 118M448).

Appendix

$$\varepsilon_{lang} = (1/2)*(C - I)$$

$$C = U^T*U = F^T*F$$

$$F = R*U$$

$$\varepsilon_{true} = Ln(U)$$

Alternatively;

$$\varepsilon_{lang} = \frac{1}{2}*(\lambda^2 - 1)$$

$$\varepsilon_{true} = Ln(\lambda)$$

where C is the right Cauchy-Green deformation tensor, I is the 2nd order identity tensor for plane stress, U is the right stretch tensor, F is the deformation gradient, R is the rotation tensor, λ is stretch ratio.

REFERENCES

[1] Benzing JT, Liu Y, Zhang X, Luecke WE, Ponge D, Dutta A, et al. Experimental and numerical study of mechanical properties of multi-phase medium-Mn TWIP-TRIP steel: influences of strain rate and phase constituents. Acta Mater 2019;177:250–65. https://doi.org/10.1016/j.actamat.2019.07.036.

[2] Wang T, Hu J, Misra RDK. Microstructure evolution and strain behavior of a medium Mn TRIP/TWIP steel for excellent combination of strength and ductility. Mater Sci Eng, A 2019;753:99–108. https://doi.org/10.1016/j.msea.2019.03.021.

[3] Depover T, Pérez Escobar D, Wallaert E, Zermout Z, Verbeken K. Effect of hydrogen charging on the mechanical

properties of advanced high strength steels. Int J Hydrogen Energy 2014;39:4647–56. https://doi.org/10.1016/j.ijhydene.2013.12.190.

[4] Bhargava M, Tewari A, Mishra SK. Forming limit diagram of Advanced High Strength Steels (AHSS) based on strain-path diagram. Mater Des 2015;85:149–55. https://doi.org/10.1016/j.matdes.2015.06.147.

[5] Callahan M, Perlade A, Schmitt JH. Interactions of negative strain rate sensitivity, martensite transformation, and dynamic strain aging in 3rd generation advanced high-strength steels. Mater Sci Eng, A 2019;754:140–51. https://doi.org/10.1016/j.msea.2019.03.042.

[6] Dwivedi SK, Vishwakarma M. Effect of hydrogen in advanced high strength steel materials. Int J Hydrogen Energy 2019;44:28007–30. https://doi.org/10.1016/j.ijhydene.2019.08.149.

[7] Bouaziz O, Allain S, Scott CP, Cugy P, Barbier D. High manganese austenitic twinning induced plasticity steels: a review of the microstructure properties relationships. Curr Opin Solid State Mater Sci 2011;15:141–68. https://doi.org/10.1016/j.cossms.2011.04.002.

[8] Gutierrez-Urrutia I, Raabe D. Dislocation and twin substructure evolution during strain hardening of an Fe–22wt.% Mn–0.6wt.% C TWIP steel observed by electron channeling contrast imaging. Acta Mater 2011;59:6449–62. https://doi.org/10.1016/j.actamat.2011.07.009.

[9] Lee SJ, Kim J, Kane SN, Cooman BC De. On the origin of dynamic strain aging in twinning-induced plasticity steels. Acta Mater 2011;59:6809–19. https://doi.org/10.1016/j.actamat.2011.07.040.

[10] Koyama M, Sawaguchi T, Tsuzaki K. Overview of dynamic strain aging and associated phenomena in Fe-Mn-C austenitic steels. ISIJ Int 2018;58:1383–95. https://doi.org/10.2355/isijinternational.ISIJINT-2018-237.

[11] Bhargava M, Chakrabarty S, Barnwal VK, Tewari A, Mishra SK. Effect of microstructure evolution during plastic deformation on the formability of transformation induced plasticity and quenched & partitioned AHSS. Mater Des 2018;152:65–77. https://doi.org/10.1016/j.matdes.2018.04.068.

[12] Bal B, Gumus B, Gerstein G, Canadinc D, Maier HJ. On the micro-deformation mechanisms active in high-manganese austenitic steels under impact loading. Mater Sci Eng, A 2015;632:29–34. https://doi.org/10.1016/j.msea.2015.02.054.

[13] Gumus B, Bal B, Gerstein G, Canadinc D, Maier HJ, Guner F, et al. Twinning activities in high-Mn austenitic steels under high-velocity compressive loading. Mater Sci Eng, A 2015;648:104–12. https://doi.org/10.1016/j.msea.2015.09.045.

[14] Chen L, Kim H-S, Kim S-K, De Cooman BC. Localized deformation due to portevin–LeChatelier effect in 18Mn–0.6C TWIP austenitic steel. ISIJ Int 2007;47:1804–12. https://doi.org/10.2355/isijinternational.47.1804.

[15] Kim JG, Hong S, Anjabin N, Park BH, Kim SK, Chin KG, et al. Dynamic strain aging of twinning-induced plasticity (TWIP) steel in tensile testing and deep drawing. Mater Sci Eng, A 2015;633:136–43. https://doi.org/10.1016/j.msea.2015.03.008.

[16] Roth A, Lebedkina TA, Lebyodkin MA. On the critical strain for the onset of plastic instability in an austenitic FeMnC steel. Mater Sci Eng, A 2012;539:280–4. https://doi.org/10.1016/j.msea.2012.01.094.

[17] Sawaguchi T, Nikulin I, Ogawa K, Sekido K, Takamori S, Maruyama T, et al. Designing Fe-Mn-Si alloys with improved low-cycle fatigue lives. Scripta Mater 2015;99:49–52. https://doi.org/10.1016/j.scriptamat.2014.11.024.

[18] Lambers HG, Rüsing CJ, Niendorf T, Geissler D, Freudenberger J, Maier HJ. On the low-cycle fatigue response of pre-strained austenitic Fe 61Mn 24Ni 6.5Cr 8.5 alloy showing TWIP effect. Int J Fatig 2012;40:51–60. https://doi.org/10.1016/j.ijfatigue.2012.01.002.

[19] Gumus B, Bal B, Gerstein G, Canadinc D, Maier HJ. Twinning activity in high-manganese austenitic steels under high velocity loading. Mater Sci Technol 2016;32:463–5. https://doi.org/10.1179/1743284715Y.0000000111.

[20] Chun YS, Kim JS, Park KT, Lee YK, Lee CS. Role of ε martensite in tensile properties and hydrogen degradation of high-Mn steels. Mater Sci Eng, A 2012;533:87–95. https://doi.org/10.1016/j.msea.2011.11.039.

[21] Jeong I, Ryu KM, Lee DG, Jung Y, Lee K, Lee JS, et al. Austenite morphology and resistance to hydrogen embrittlement in medium Mn transformation-induced plasticity steel. Scripta Mater 2019;169:52–6. https://doi.org/10.1016/j.scriptamat.2019.05.011.

[22] Grässel O, Krüger L, Frommeyer G, Meyer LW. High strength Fe-Mn-(Al, Si) TRIP/TWIP steels development - properties - application. Int J Plast 2000;16:1391–409. https://doi.org/10.1016/S0749-6419(00)00015-2.

[23] Kusakin PS, Kaibyshev RO. High-Mn twinning-induced plasticity steels: microstructure and mechanical properties. Rev Adv Mater Sci 2016;44:326–60.

[24] Bal B, Gumus B, Canadinc D. Incorporation of dynamic strain aging into a viscoplastic self-consistent model for predicting the negative strain rate sensitivity of hadfield steel. J Eng Mater Technol Trans ASME 2016;138:1–8. https://doi.org/10.1115/1.4033072.

[25] Fu X, Wu X, Yu Q. Dislocation plasticity reigns in a traditional twinning-induced plasticity steel by in situ observation. Mater Today Nano 2018;3:48–53. https://doi.org/10.1016/j.mtnano.2018.11.004.

[26] Jeong K, Jin J-E, Jung Y-S, Kang S, Lee Y-K. The effects of Si on the mechanical twinning and strain hardening of Fe–18Mn–0.6C twinning-induced plasticity steel. Acta Mater 2013;61:3399–410. https://doi.org/10.1016/j.actamat.2013.02.031.

[27] Koyama M, Akiyama E, Lee YK, Raabe D, Tsuzaki K. Overview of hydrogen embrittlement in high-Mn steels. Int J Hydrogen Energy 2017;42:12706–23. https://doi.org/10.1016/j.ijhydene.2017.02.214.

[28] Hong S, Lee J, Lee B, Seop H, Kim S, Chin K, et al. Effects of intergranular carbide precipitation on delayed fracture behavior in three TWinning Induced Plasticity (TWIP) steels. Mater Sci Eng, A 2013;587:85–99. https://doi.org/10.1016/j.msea.2013.08.063.

[29] Ronevich JA, Kim SK, Speer JG, Matlock DK. Hydrogen effects on cathodically charged twinning-induced plasticity steel. Scripta Mater 2012;66:956–9. https://doi.org/10.1016/j.scriptamat.2011.12.012.

[30] Bai Y, Momotani Y, Chen MC, Shibata A, Tsuji N. Effect of grain refinement on hydrogen embrittlement behaviors of high-Mn TWIP steel. Mater Sci Eng, A 2016;651:935–44. https://doi.org/10.1016/j.msea.2015.11.017.

[31] Koyama M, Akiyama E, Tsuzaki K, Raabe D. Hydrogen-assisted failure in a twinning-induced plasticity steel studied under in situ hydrogen charging by electron channeling contrast imaging. Acta Mater 2013;61:4607–18. https://doi.org/10.1016/j.actamat.2013.04.030.

[32] Lee SM, Park IJ, Jung JG, Lee YK. The effect of Si on hydrogen embrittlement of Fe-18Mn-0.6C-xSi twinning-induced plasticity steels. Acta Mater 2016;103:264–72. https://doi.org/10.1016/j.actamat.2015.10.015.

[33] Tuğluca IB, Koyama M, Shimomura Y, Bal B, Canadinc D, Akiyama E, et al. Lowering strain rate simultaneously enhances carbon- and hydrogen-induced mechanical degradation in an Fe-33Mn-1.1C steel. Metall Mater Trans A Phys Metall Mater Sci 2019;50:1137–41. https://doi.org/10.1007/s11661-018-5080-7.

[34] Nikulin I, Sawaguchi T, Tsuzaki K. Effect of alloying composition on low-cycle fatigue properties and

microstructure of Fe–30Mn–(6–x)Si–xAl TRIP/TWIP alloys. Mater Sci Eng, A 2013;587:192–200. https://doi.org/10.1016/j.msea.2013.08.061.

[35] Wang D, Lu X, Deng Y, Guo X, Barnoush A. Effect of hydrogen on nanomechanical properties in Fe-22Mn-0.6C TWIP steel revealed by in-situ electrochemical nanoindentation. Acta Mater 2019;166:618–29. https://doi.org/10.1016/j.actamat.2018.12.055.

[36] Kwon YJ, Lee T, Lee J, Chun YS, Lee CS. Role of Cu on hydrogen embrittlement behavior in Fe-Mn-C-Cu TWIP steel. Int J Hydrogen Energy 2015;40:7409–19. https://doi.org/10.1016/j.ijhydene.2015.04.022.

[37] Najam H, Koyama M, Bal B, Akiyama E, Tsuzaki K. Strain rate and hydrogen effects on crack growth from a notch in a Fe-high-Mn steel containing 1.1 wt% solute carbon. Int J Hydrogen Energy 2020;45:1125–39. https://doi.org/10.1016/j.ijhydene.2019.10.227.

[38] Tuğluca IB, Koyama M, Bal B, Canadinc D, Akiyama E, Tsuzaki K. High-concentration carbon assists plasticity-driven hydrogen embrittlement in a Fe-high Mn steel with a relatively high stacking fault energy. Mater Sci Eng, A 2018;717:78–84. https://doi.org/10.1016/j.msea.2018.01.087.

[39] Koyama M, Akiyama E, Tsuzaki K. Effects of static and dynamic strain aging on hydrogen embrittlement in twip steels containing al. ISIJ Int 2013;53:1268–74. https://doi.org/10.2355/isijinternational.53.1268.

[40] Michler T, San Marchi C, Naumann J, Weber S, Martin M. Hydrogen environment embrittlement of stable austenitic steels. Int J Hydrogen Energy 2012;37:16231–46. https://doi.org/10.1016/j.ijhydene.2012.08.071.

[41] Bal B, Koyama M, Gerstein G, Maier HJ, Tsuzaki K. Effect of strain rate on hydrogen embrittlement susceptibility of twinning-induced plasticity steel pre-charged with high-pressure hydrogen gas. Int J Hydrogen Energy 2016;41:15362–72. https://doi.org/10.1016/j.ijhydene.2016.06.259.

[42] Chung K, Ahn K, Yoo DH, Chung KH, Seo MH, Park SH. Formability of TWIP (twinning induced plasticity) automotive sheets. Int J Plast 2011;27:52–81. https://doi.org/10.1016/j.ijplas.2010.03.006.

[43] Folgar RH, Böddeker T, Chergui A, Ivanjko M, Gili F, Behrens S. Joining TWIP-steel simulation models. Procedia Struct Integr 2017;5:516–23. https://doi.org/10.1016/j.prostr.2017.07.154.

[44] Xu L, Barlat F, Lee MG. Hole expansion of twinning-induced plasticity steel. Scripta Mater 2012;66:1012–7. https://doi.org/10.1016/j.scriptamat.2012.01.062.

[45] Lorthios J, Mazière M, Lemoine X, Cugy P, Besson J, Gourgues-Lorenzon AF. Fracture behaviour of a Fe-22Mn-0.6C-0.2V austenitic TWIP steel. Int J Mech Sci 2015;101–102:99–113. https://doi.org/10.1016/j.ijmecsci.2015.07.029.

[46] Hardie D, Liu S. The effect of stress concentration on hydrogen embrittlement of a low alloy steel. Corrosion Sci 1996;38:721–33. https://doi.org/10.1016/0010-938X(96)00161-8.

[47] Li Y, Wierzbicki T. Prediction of plane strain fracture of AHSS sheets with post-initiation softening. Int J Solid Struct 2010;47:2316–27. https://doi.org/10.1016/j.ijsolstr.2010.04.028.

[48] Fabrègue D, Landron C, Bouaziz O, Maire E. Damage evolution in TWIP and standard austenitic steel by means of 3D X ray tomography. Mater Sci Eng, A 2013;579:92–8. https://doi.org/10.1016/j.msea.2013.05.013.

[49] Enos DG, Scully JR. A critical-strain criterion for hydrogen embrittlement of cold-drawn, ultrafine pearlitic steel. Metall Mater Trans A Phys Metall Mater Sci 2002;33:1151–66. https://doi.org/10.1007/s11661-002-0217-z.

[50] Wang MQ, Akiyama E, Tsuzaki K. Fracture criterion for hydrogen embrittlement of high strength steel. Mater Sci Technol 2006;22:167–72. https://doi.org/10.1179/174328406X86191.

[51] Wang M, Akiyama E, Tsuzaki K. Effect of hydrogen on the fracture behavior of high strength steel during slow strain rate test. Corrosion Sci 2007;49:4081–97. https://doi.org/10.1016/j.corsci.2007.03.038.

[52] Wang M, Akiyama E, Tsuzaki K. Crosshead speed dependence of the notch tensile strength of a high strength steel in the presence of hydrogen. Scripta Mater 2005;53:713–8. https://doi.org/10.1016/j.scriptamat.2005.05.014.

[53] Yu H, Olsen JS, Alvaro A, Olden V, He J, Zhang Z. A uniform hydrogen degradation law for high strength steels. Eng Fract Mech 2016;157:56–71. https://doi.org/10.1016/j.engfracmech.2016.02.001.

[54] Ahn DC, Sofronis P, Dodds R. Modeling of hydrogen-assisted ductile crack propagation in metals and alloys. Int J Fract 2007;145:135–57. https://doi.org/10.1007/s10704-007-9112-3.

[55] Bal B, Okdem B, Bayram FC, Aydin M. A detailed investigation of the effect of hydrogen on the mechanical response and microstructure of Al 7075 alloy under medium strain rate impact loading. Int J Hydrogen Energy 2020;45(46):25509–22. https://doi.org/10.1016/j.ijhydene.2020.06.241.

[56] Kwon YJ, Jung SP, Lee BJ, Lee CS. Grain boundary engineering approach to improve hydrogen embrittlement resistance in Fe-Mn-C TWIP steel. Int J Hydrogen Energy 2018;43:10129–40. https://doi.org/10.1016/j.ijhydene.2018.04.048.

[57] McClintock FA. A criterion for ductile fracture by the growth of holes. J Appl Mech 1968;35:363–71. https://doi.org/10.1115/1.3601204.

[58] Rice JR, Tracey DM. On the ductile enlargement of voids in triaxial stress fields*. J Mech Phys Solid 1969;17:201–17. https://doi.org/10.1016/0022-5096(69)90033-7.

[59] Bai Y, Teng X, Wierzbicki T. On the application of stress triaxiality formula for plane strain fracture testing. J Eng Mater Technol Trans ASME 2009;131:021002. https://doi.org/10.1115/1.3078390.

[60] Basu S, Benzerga AA. On the path-dependence of the fracture locus in ductile materials: Experiments. Int J Solid Struct 2015;71:79–90. https://doi.org/10.1016/j.ijsolstr.2015.06.003.

[61] Johnson GR, Cook WH. Fracture characteristics of three metals subjected to various strains, strain rates, temperatures and pressures. Eng Fract Mech 1985;21:31–48. https://doi.org/10.1016/0013-7944(85)90052-9.

[62] Bridgman PW. In: Studies in large plastic flow and fracture, vol. 115. Cambridge, MA and London, England: Harvard University Press; 1964. https://doi.org/10.4159/harvard.9780674731349.

[63] Alves M, Jones N. Influence of hydrostatic stress on failure of axisymmetric notched specimens. J Mech Phys Solid 1999;47:643–67. https://doi.org/10.1016/S0022-5096(98)00060-X.

[64] Goolsby RD, Chatterjee AM. Notch sensitivity and fractography of polyolefins. Polym Eng Sci 1983;23:117–24. https://doi.org/10.1002/pen.760230303.

[65] Sobieraj MC, Kurtz SM, Rimnac CM. Notch sensitivity of PEEK in monotonic tension. Biomaterials 2009;30:6485–94. https://doi.org/10.1016/j.biomaterials.2009.08.020.

[66] Blaber J, Adair B, Antoniou A. Ncorr: open-source 2D digital image correlation matlab software. Exp Mech 2015;55:1105–22. https://doi.org/10.1007/s11340-015-0009-1.

[67] Seymen Y, Güler B, Efe M. Large strain and small-scale biaxial testing of sheet metals. Exp Mech 2016;56:1519–30. https://doi.org/10.1007/s11340-016-0185-7.

[68] Lee S, Kim J, Lee S-J, De Cooman BC. Effect of nitrogen on the critical strain for dynamic strain aging in high-manganese twinning-induced plasticity steel. Scripta Mater 2011;65:528–31. https://doi.org/10.1016/j.scriptamat.2011.06.017.

[69] Koyama M, Sawaguchi T, Tsuzaki K. TWIP effect and plastic instability condition in an Fe-Mn-C austenitic steel. ISIJ Int 2013;53:323–9. https://doi.org/10.2355/isijinternational.53.323.

[70] Koyama M, Tasan CC, Akiyama E, Tsuzaki K, Raabe D. Hydrogen-assisted decohesion and localized plasticity in dual-phase steel. Acta Mater 2014;70:174–87. https://doi.org/10.1016/j.actamat.2014.01.048.

[71] Choung J, Nam W, Lee D, Song CY. Failure strain formulation via average stress triaxiality of an EH36 high strength steel. Ocean Eng 2014;91:218–26. https://doi.org/10.1016/j.oceaneng.2014.09.019.

[72] Wan D, Deng Y, Meling JIH, Alvaro A, Barnoush A. Hydrogen-enhanced fatigue crack growth in a single-edge notched tensile specimen under in-situ hydrogen charging inside an environmental scanning electron microscope. Acta Mater 2019;170:87–99. https://doi.org/10.1016/j.actamat.2019.03.032.

[73] Yin Q, Soyarslan C, Isik K, Tekkaya AE. A grooved in-plane torsion test for the investigation of shear fracture in sheet materials. Int J Solid Struct 2015;66:121–32. https://doi.org/10.1016/j.ijsolstr.2015.03.032.

[74] Koyama M, Akiyama E, Tsuzaki K. Hydrogen embrittlement in a Fe-Mn-C ternary twinning-induced plasticity steel. Corrosion Sci 2012;54:1–4. https://doi.org/10.1016/j.corsci.2011.09.022.

[75] Park IJ, Jeong KH, Jung JG, Lee CS, Lee YK. The mechanism of enhanced resistance to the hydrogen delayed fracture in Al-added Fe-18Mn-0.6C twinning-induced plasticity steels. Int J Hydrogen Energy 2012;37:9925–32. https://doi.org/10.1016/j.ijhydene.2012.03.100.

[76] Luo H, Li Z, Raabe D. Hydrogen enhances strength and ductility of an equiatomic high-entropy alloy. Sci Rep 2017;7:1–7. https://doi.org/10.1038/s41598-017-10774-4.

[77] Barbier D, Gey N, Allain S, Bozzolo N, Humbert M. Analysis of the tensile behavior of a TWIP steel based on the texture and microstructure evolutions. Mater Sci Eng, A 2009;500:196–206. https://doi.org/10.1016/j.msea.2008.09.031.

[78] Renard K, Jacques PJ. On the relationship between work hardening and twinning rate in TWIP steels. Mater Sci Eng, A 2012;542:8–14. https://doi.org/10.1016/j.msea.2012.01.123.

[79] Shen YF, Qiu CH, Wang L, Sun X, Zhao XM, Zuo L. Effects of cold rolling on microstructure and mechanical properties of Fe-30Mn-3Si-4Al-0.093C TWIP steel. Mater Sci Eng, A 2013;561:329–37. https://doi.org/10.1016/j.msea.2012.10.020.

[80] Olson GB, Cohen M. Kinetics of strain-induced martensitic nucleation. Metall Trans A 1975;6:791–5. https://doi.org/10.1007/BF02672301.

[81] Li X, Gong B, Deng C, Li Y. Failure mechanism transition of hydrogen embrittlement in AISI 304 K-TIG weld metal under tensile loading. Corrosion Sci 2018;130:241–51. https://doi.org/10.1016/j.corsci.2017.10.032.

[82] Lou X, Andresen PL, Rebak RB. Oxide inclusions in laser additive manufactured stainless steel and their effects on impact toughness and stress corrosion cracking behavior. J Nucl Mater 2018;499:182–90. https://doi.org/10.1016/j.jnucmat.2017.11.036.

[83] Díaz A, Alegre JM, Cuesta II. A review on diffusion modelling in hydrogen related failures of metals. Eng Fail Anal 2016;66:577–95. https://doi.org/10.1016/j.engfailanal.2016.05.019.

[84] Bai Y, Tian Y, Gao S, Shibata A, Tsuji N. Hydrogen embrittlement behaviors of ultrafine-grained 22Mn-0.6C austenitic twinning induced plasticity steel. J Mater Res 2017;32:4592–604. https://doi.org/10.1557/jmr.2017.351.

[85] Kameda J, McMahon CJ. Solute segregation and hydrogen-induced intergranular fracture in an alloy steel. Metall Trans A, Phys Metall Mater Sci 1983;14 A:903–11. https://doi.org/10.1007/BF02644295.

[86] Yamaguchi M, Ebihara KI, Itakura M, Kadoyoshi T, Suzudo T, Kaburaki H. First-principles study on the grain boundary embrittlement of metals by solute segregation: Part II. metal (Fe, Al, Cu)-hydrogen (H) systems. Metall Mater Trans A Phys Metall Mater Sci 2011;42:330–9. https://doi.org/10.1007/s11661-010-0380-6.

[87] Liu Q, Zhou Q, Venezuela J, Zhang M, Atrens A. The role of the microstructure on the influence of hydrogen on some advanced high-strength steels. Mater Sci Eng, A 2018;715:370–8. https://doi.org/10.1016/j.msea.2017.12.079.

[88] Dadfarnia M, Novak P, Ahn DC, Liu JB, Sofronis P, Johnson DD, et al. Recent advances in the study of structural materials compatibility with hydrogen. Adv Mater 2010;22:1128–35. https://doi.org/10.1002/adma.200904354.

[89] Liu Q, Zhou Q, Venezuela J, Zhang M, Wang J, Atrens A. A review of the influence of hydrogen on the mechanical properties of DP, TRIP, and TWIP advanced high-strength steels for auto construction. Corrosion Rev 2016;34:127–52. https://doi.org/10.1515/corrrev-2015-0083.

[90] Bao Y, Wierzbicki T. On fracture locus in the equivalent strain and stress triaxiality space. Int J Mech Sci 2004;46:81–98. https://doi.org/10.1016/j.ijmecsci.2004.02.006.

[91] Qian L, Wang X, Sun C, Dai A. Correlation of macroscopic fracture behavior with microscopic fracture mechanism for AHSS sheet. Materials 2019;16:900. https://doi.org/10.3390/ma12060900.